JOURNAL OF AIRCRAFT
Vol. 30, No. 5, Sept.–Oct. 1993

Finite State Aeroelastic Model for Use in Rotor Design Optimization

Chengjian He* and David A. Peters†
Georgia Institute of Technology, Atlanta, Georgia 30332

In this article, a rotor aeroelastic model based on a newly developed finite state dynamic wake, coupled with blade finite element analysis, is described. The analysis is intended for application in rotor blade design optimization. A coupled simultaneous system of differential equations combining blade structural dynamics and aerodynamics is established in a formulation well-suited for design sensitivity computation. Each blade is assumed to be an elastic beam undergoing flap bending, lead-lag bending, elastic twist, and axial deflections. Aerodynamic loads are computed from unsteady blade element theory where the rotor three-dimensional unsteady wake is described by a generalized dynamic wake model. Correlation of results obtained from the analysis with flight test data is provided to assess model accuracy.

Nomenclature

a	=	slope of lift curve, 5.73
b	=	blade semichord, m
C_n	=	blade sectional normal force coefficient
C_T	=	rotor thrust coefficient
c	=	blade chord, m
c_d	=	blade sectional drag coefficient
e_d	=	chordwise offset of aerodynamic center from elastic axis, m
e_0	=	distance between elastic axis and midchord, m
R	=	rotor radius, m
t	=	time, s
$\bar{t}$	=	nondimensional time, Ωt, rad
r	=	blade radial station, dimensionless on R
x_{ac}	=	distance from leading edge to aerodynamic center, m
α_n^m, β_n^m	=	induced flow states
η_c	=	$0.75c - x_{ac} - e_d$
θ	=	blade pitch, rad
θ_c	=	collective pitch, deg
θ_{1c}	=	lateral cyclic pitch, deg
θ_{1s}	=	longitudinal cyclic pitch, deg
λ_i	=	induced inflow at rotor disk, m/s
μ	=	advance ratio
ρ	=	air density, kg/m^3
σ	=	rotor solidity
Ω	=	rotor rotational speed, rad/s
ω_i	=	blade ith mode natural frequency, dimensionless on Ω
$*$	=	$d/d\bar{t}$
$**$	=	$d^2/d\bar{t}^2$

Introduction

INTEGRATED multidisciplinary rotorcraft optimization requires systematic analyses of aerodynamics, dynamics, and structures. Since there are large numbers of design constraints and design variables involved, this requires an intensive numerical computation. Furthermore, usually a large number of iterations is needed before an optimum solution is achieved. Therefore, a rotor aeroelastic model appropriate to multidisciplinary optimization should be computationally efficient with reasonable accuracy. For computational efficiency, a formulation is needed that is well-suited for the design sensitivity calculation, which is a most time-consuming part of optimization. Although a finite difference technique may be used in this aspect, its computation time is often formidable in rotorcraft analysis. This is especially true in forward flight with a rotor wake in consideration for which even a single run can take a significant computational effort.

Through many years of development, a number of tools have become available for rotorcraft aeroelastic analysis.[1–6] Based on these or comparable analyses, Refs. 7–9 perform aeroelastic tailoring to reduce vehicle vibration. Reference 10 includes both aerodynamic and structural dynamic design variables in an aeroelastic design process. When aerodynamic design variables, such as blade planform and twist, are included as independent design variables, this requires a consistent modeling for the interaction between aerodynamics and dynamics. In particular, when the rotor wake or other nonlinear aerodynamic properties are coupled in the analysis, one needs to perturb explicitly the aerodynamics (wake or dynamic stall) with respect to the design variables during the design process.

In this article, a generalized dynamic wake[11,12] is combined with blade finite elements to form a finite state aeroelastic model intended for such an optimization design application. The analysis offers a unique formulation of a coupled system with simultaneous blade dynamics and aerodynamics. With this formulation, not only dynamic response, but also design derivatives can be computed directly from a simultaneous solution of a system of ordinary differential equations for both blade dynamics and aerodynamics. Thus, both blade dynamic and aerodynamic variations due to design change can be evaluated explicitly and efficiently. For verification, the calculated results from this model are compared with measured data of a SA349/2 helicopter.[13]

Blade Finite Elements

The finite element method is applied to the blade structural modeling. The blade element has 12 degrees of freedom (DOF) which include three rectilinear and three rotational displacements at each end. The nonuniform EI, GJ is assumed as a linear distribution over each element. In the present analysis, 14 elements have been used, which gives satisfactory results for blade natural frequencies and mode shapes.

The stiffness matrix of the equations is obtained from a strain energy expression that contains the contributions from in-plane and out-of-plane bending, torsion, and axial deformation.[14] The potential energy due to the tension and elastic twist induced by the centrifugal force field and due to torsion is also included; but no cross-sectional warping is considered

Received June 17, 1991; revision received June 26, 1992; accepted for publication July 1, 1992.

*Postdoctoral Fellow. Member AIAA.
†Professor. Fellow AIAA.

since this analysis is not for composite beam, and thus these errors are negligible. The center of gravity (c.g.) does not coincide with the elastic axis. Therefore, there is an inertial coupling between torsion and out-of-plane bending. For the computation of blade natural frequency and mode shapes, the mass is further assumed to be concentrated at nodes; but the exact inertia terms, including Coriolis terms, are included in the blade equations of motion.[3]

In forward flight, the equations of blade motion are time-dependent. For an efficient computation, the normal modes are utilized to separate time and space dependency. Thus, the complicated blade dynamics equations are simplified by converting them into the modal domain in the form of normal modal equations.

Aerodynamics

Aerodynamic loadings that drive the blade motion are obtained from an unsteady aerodynamic theory. In this theory, the airloads are computed from unsteady airfoil elements and contain the influence of the rotor unsteady wake from a finite state wake.[11,12] In the derivation of these aerodynamic force expressions, relationships are formed between the undeformed blade coordinate system (x, y, z with unit vectors $\boldsymbol{i}$, $\boldsymbol{j}$, $\boldsymbol{k}$) and the deformed blade coordinate system (ξ, η, ζ with unit vectors $\boldsymbol{i}_\xi$, $\boldsymbol{j}_\eta$, $\boldsymbol{k}_\zeta$), Fig. 1.

A point on the undeformed elastic axis undergoes deflection u, v, w in the x, y, z directions. Then the blade cross section undergoes a rotation θ_T about the deformed elastic axis. A total blade pitch θ_T is defined as

$$\theta_T = \theta + \phi \tag{1}$$

where θ is blade control pitch, and ϕ is elastic torsion.

The coordinate transformation between the deformed and the undeformed blade coordinate system can be found in Ref. 3.

Relative Airflow

The airloads are formulated in the deformed blade frame. The airflow velocity due to the blade motion, the forward flight speed, and the rotor wake are first obtained in the undeformed blade frame. Then, with the transformation, the air velocity can be written in the deformed blade frame

$$\boldsymbol{U} = U_\xi \boldsymbol{i}_\xi + U_\eta \boldsymbol{j}_\eta + U_\zeta \boldsymbol{k}_\zeta \tag{2}$$

The expressions for U_ξ, U_η, and U_ζ are lengthy, interested readers can refer to Ref. 15 for detailed information.

In the calculation of the relative airflow normal to the blade segment, the chordwise variation and effects of an arbitrary camber line of the airfoil are retained. This is necessary due to the fact that the relative airflow at the $\frac{3}{4}$ chord point is not always sufficient for the blade sectional lift, moment, and drag

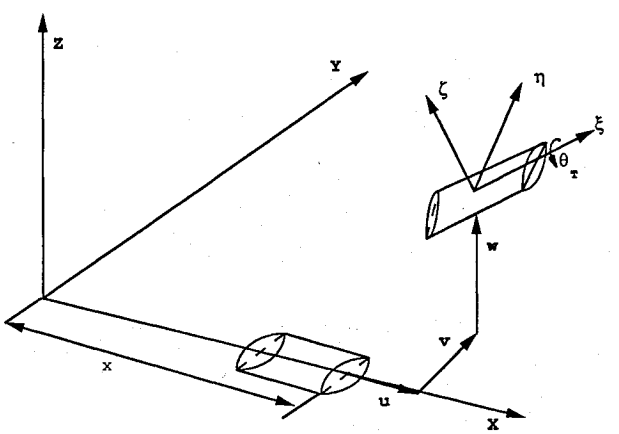

Fig. 1 Transformation geometry.

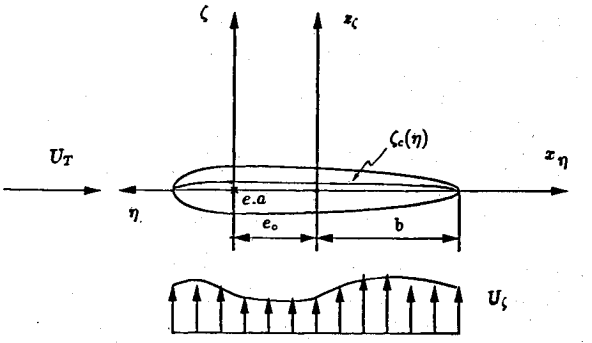

Fig. 2 Airfoil configuration.

computation. Since both the chordwise and camberwise variations of radial and tangential relative airflow are negligible in aerodynamic force calculations, to simplify the computation, we use the radial and tangential components of the airflow at the $\frac{3}{4}$ chord point, i.e.

$$U_R = -U_\xi|_{\eta=\eta_c} \tag{3}$$

$$U_T = -U_\eta|_{\eta=\eta_c} \tag{4}$$

Airloads Theory

As shown in Fig. 2, to satisfy the condition of no airflow through the airfoil, we have the integral equation for bound vorticity distribution γ

$$U_\zeta(x_\eta) = \frac{1}{2\pi}\int_{-b}^{+b} \frac{\gamma(\xi)}{x_\eta - \xi}\,\mathrm{d}\xi \tag{5}$$

where $x_\eta = -(\eta + e_0)$, and U_ζ is total inflow which includes both the inflow due to blade motion and induced flow due to wake (excluding bound vorticity). Therefore, we can write

$$U_\zeta = w_b(x_\eta) - \lambda_i(x_\eta) \tag{6}$$

where w_b is the relative airflow due to blade motions, and λ_i is the wake-induced inflow. The three-dimensional unsteady induced flow from the generalized dynamic wake theory is utilized here to replace Theodorsen's simple two-dimensional single-layer flat wake. Thus, the resultant airloads are both three-dimensional and unsteady, which is better suited for rotor aeroelasticity studies than conventional two-dimensional theory with only uniform, or Dree's induced inflow.

Using a basic transformation $x_\eta = b\cos\theta_\xi$, we can expand U_ζ in a Fourier series across the airfoil chord

$$U_\zeta(x_\eta) = \sum_{n=0}^{\infty} w_n \cos(n\theta_\xi) \tag{7}$$

where $w_n = w_{bn} - \lambda_{in}$ with

$$w_{b0} = \frac{1}{\pi}\int_0^\pi w_b\,\mathrm{d}\theta_\xi \tag{8}$$

$$\lambda_{i0} = \frac{1}{\pi}\int_0^\pi \lambda_i\,\mathrm{d}\theta_\xi \tag{9}$$

$$w_{bn} = \frac{2}{\pi}\int_0^\pi w_b \cos(n\theta_\xi)\,\mathrm{d}\theta_\xi \quad n \neq 0 \tag{10}$$

$$\lambda_{in} = \frac{2}{\pi}\int_0^\pi \lambda_i \cos(n\theta_\xi)\,\mathrm{d}\theta_\xi \quad n \neq 0 \tag{11}$$

Further detailed expressions for w_{bn} are given in Ref. 15. The λ_{in} are determined from the wake theory that will be discussed in the following section.

Combining blade sectional lift with the profile drag, we obtain the blade sectional aerodynamic loads in the deformed blade frame as

$$\hat{L}_u^a = -\tfrac{1}{2}\rho c c_d U U_R \tag{12}$$

$$\hat{L}_v^a = \tfrac{1}{2}\rho c\{a(w_{b0} - \lambda_{i0})[(w_{b0} - \lambda_{i0}) + \tfrac{1}{2}(w_{b1} - \lambda_{i1})] - c_d U_T U\} \tag{13}$$

$$\hat{L}_w^a = \tfrac{1}{2}\rho c\{aU_T[(w_{b0} - \lambda_{i0}) + \tfrac{1}{2}w_{b1}] + (\pi c/2)(\dot{w}_{b0} - \tfrac{1}{2}\dot{w}_{b2}) + c_d(w_{b0} - \lambda_{i0})U\} \tag{14}$$

$$\hat{M}_\phi^a = \tfrac{1}{4}\rho c^2\{(a/2)U_T(w_{b0} - \lambda_{i0} - \tfrac{1}{2}w_{b2}) - (\pi/8)b(\dot{w}_{b1} - \dot{w}_{b3})\} - e_0\tfrac{1}{2}\rho c\{aU_T[(w_{b0} - \lambda_{i0}) + \tfrac{1}{2}w_{b1}] + \pi b(\dot{w}_{b0} - \tfrac{1}{2}\dot{w}_{b2})\} \tag{15}$$

Since the blade equations of motion are established in the undeformed frame, these airloads must be transformed to the undeformed blade frame.

Three-Dimensional Unsteady Wake

The generalized dynamic wake theory[11,12] is utilized for airload computations. In this theory, the unsteady induced flow is related to the blade circulatory aerodynamic loads by a set of first-order ordinary differential equations

$$[M^c]\{\alpha_n^m\}^* + [L^c]^{-1}\{\alpha_n^m\} = \{\tau_n^{mc}\} \tag{16}$$

$$[M^s]\{\beta_n^m\}^* + [L^s]^{-1}\{\beta_n^m\} = \{\tau_n^{ms}\} \tag{17}$$

where α_n^m and β_n^m are the induced flow expansion coefficients

$$\frac{\lambda_i(r, \psi, \bar{t})}{\Omega R} = \sum_{m=0}^{\infty} \sum_{n=m+1,m+3,\ldots}^{\infty} \phi_n^m(r)[\alpha_n^m(\bar{t})\cos(m\psi) + \beta_n^m(\bar{t})\sin(m\psi)] \tag{18}$$

where $\phi_n^m(r)$ are the induced inflow radial shape functions, which are simple polynomials in r.[12] The coefficient matrices in Eqs. (16) and (17) are available in analytical closed form.[12] The τ_n^{mc} and τ_n^{ms} are inflow forcing functions also discussed in Ref. 12. They can be computed from blade sectional circulatory lift L_q which can be obtained from unsteady lift theory, as described in the previous section

$$L_q = (\rho c/2)aU_T[(w_{b0} - \lambda_{i0}) + \tfrac{1}{2}(w_{b1} - \lambda_{i1})] \tag{19}$$

with λ_{i0} and λ_{i1} from integrals of the induced flow across the blade chord [Eqs. (9) and (11)].

Solution Methodology

The blade response is solved from combined blade and inflow dynamic equations. The blade dynamic equations of motion are

$$[M]\{\overset{**}{X}\} + [C]\{\overset{*}{X}\} + [K]\{X\} = \{F\} \tag{20}$$

where F are external nodal forces. The (*) is a derivative with respect to nondimensional time. Using normal modes, we can expand the nodal displacements in terms of generalized coordinates q

$$\{X\} = [\Phi]\{q\} \tag{21}$$

Then, we obtain the differential equations for blade q

$$\{\overset{**}{q}\} + [\omega_i^2]\{q\} = [\Phi]^T(\{F\} - [C][\Phi]\{\overset{*}{q}\}) \equiv \{f\} \tag{22}$$

The above equations are rearranged to offer first-order state equations that are combined with induced flow equations [Eqs. (16 and 17)] and autopilot equations,[5] to form the final set of system equations. Then, a fourth-order Runge-Kutta integration scheme is applied for a time-marching solution

$$[D]\begin{Bmatrix} \{\overset{*}{q}\} \\ \{q\} \\ \{\alpha_n^m\} \\ \{\beta_n^m\} \\ \{\overset{*}{\theta}\} \\ \{\theta\} \end{Bmatrix}^* + [E]\begin{Bmatrix} \{\overset{*}{q}\} \\ \{q\} \\ \{\alpha_n^m\} \\ \{\beta_n^m\} \\ \{\overset{*}{\theta}\} \\ \{\theta\} \end{Bmatrix} = \begin{Bmatrix} \{f\} \\ \{0\} \\ \{\tau_n^{mc}\} \\ \{\tau_n^{ms}\} \\ \Delta C_T \\ \Delta\beta_c \\ \Delta\beta_s \\ \{0\} \end{Bmatrix} \tag{23}$$

where $[D]$ and $[E]$ are assembled from blade dynamics, inflow dynamics, and autopilot equations.[15] The ΔC_T is the difference between current thrust coefficient and the desired one, and similarly, the $\Delta\beta_c$ and $\Delta\beta_s$ are the deviations to the desired rotor cyclic flapping.

Results and Discussion

The numerical loads and response results are correlated with flight test data from Ref. 13. A modified Aerospatiale Gazelle SA349/2 helicopter was used in the flight test. It is a three-bladed rotor with −7.3-deg built-in pretwist. Both the structural and aerodynamic characteristic used in the computation are given in Ref. 13. The results are calculated for three forward flight conditions at advance ratios of 0.14, 0.198, and 0.344 with $C_T/\sigma = 0.064$.

Trim

For blade dynamic response, six coupled modes have been used. These include the first to third flapping, the first and second lag, and the first torsion. They cover a natural frequency range from 0.43 to 5.30/rev. Therefore, we use corresponding inflow states up to the sixth harmonic with 28 inflow states total. The time marching starts with an estimated trim setting based on simple momentum and blade element theory with rigid blades,[16] and stops after a steady periodic solution is obtained. The autopilot controller trims the rotor to a desired rotor thrust, and a desired tip-path-plane orientation. This trim analysis can also be extended to full free-flight analysis without formulation change.[5] Each run has 70 states in total (36 for structural dynamics, 28 for inflow dynamics, and 6 for autopilot) and takes only about 85 s to complete on the Cyber 990 at the Georgia Tech computer center. This is much less than that required to do the same analysis with a free or prescribed wake, and it is sufficiently small to allow optimization[17] because a direct solution of design sensitivity can be obtained from the rotor aeroelastic equations without resorting to finite difference.

Table 1 shows the correlation of blade trim settings between theory and experiment. For $\mu = 0.14$, both collective and lateral cyclic pitch are within 0.5-deg agreement, but the longitudinal pitch differs by 0.91 deg, possibly due to flow over the fuselage. We have not included flow over the fuselage which could account for part of the difference. There is no blockage at this advance ratio. For $\mu = 0.198$, collective pitch differs by 0.93 deg, while both cyclic pitch angle are close to flight test data with an error of 0.5 deg or less. For the higher advance ratio, $\mu = 0.344$, the main difference is that predicted collective pitch is about 3.8 deg less than measured. The differences could be possibly due to elastic torsion response, which is not well-predicted in the current theory due to the assumption of lifting-line aerodynamics. Overall, the autopilot has done a satisfactory job of trimming, but lack of advanced aerodynamics and fuselage influence introduces trim errors that are accentuated with increasing advance ratio.

Figure 3 depicts blade tip flapping response. The calculated results and measured data have a close agreement for the two lower speed flight conditions. This is not surprising because the tip-path-plane orientation is the trim objective. Thus, the predicted total 1/rev torsion (elastic plus trim) must match

Table 1 Comparison of control settings

	μ = 0.14		μ = 0.198		μ = 0.349	
Item	Theory	Data	Theory	Data	Theory	Data
θ_c	6.43 deg	6.94 deg	6.30 deg	7.23 deg	8.16 deg	11.97 deg
θ_{1c}	0.92 deg	1.39 deg	0.96 deg	1.22 deg	1.72 deg	2.19 deg
θ_{1s}	0.57 deg	1.48 deg	−0.71 deg	−0.21 deg	−4.58 deg	−5.95 deg

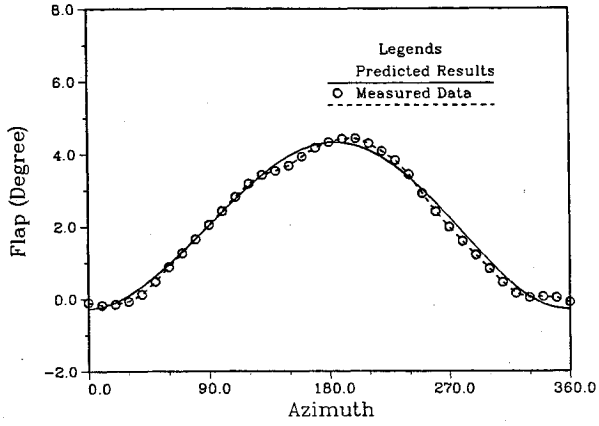

a) C_T = 0.0042, μ = 0.14

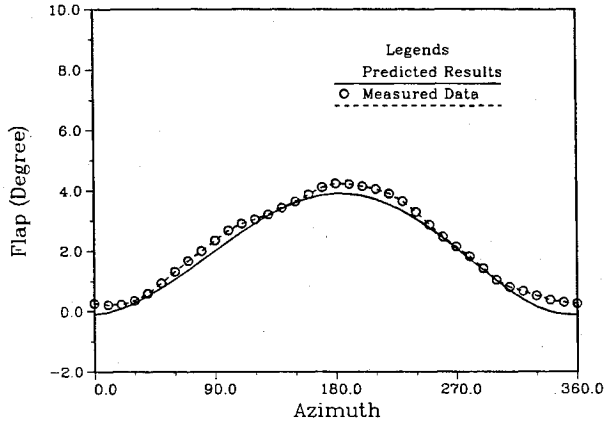

b) C_T = 0.0042, μ = 0.198

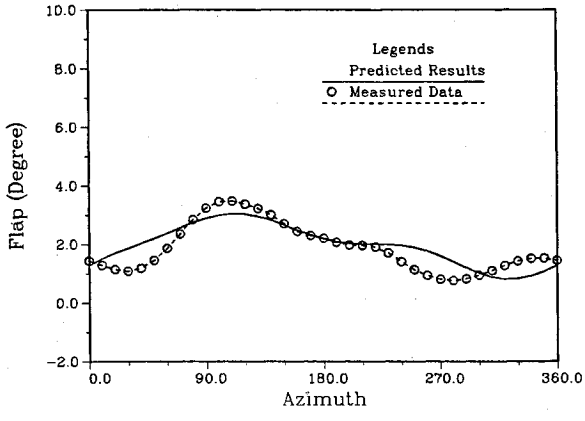

c) C_T = 0.0040, μ = 0.344

Fig. 3 Blade flapping response.

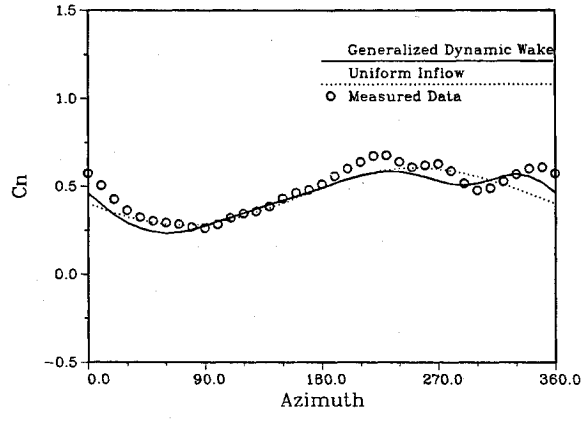

a) r = 0.75

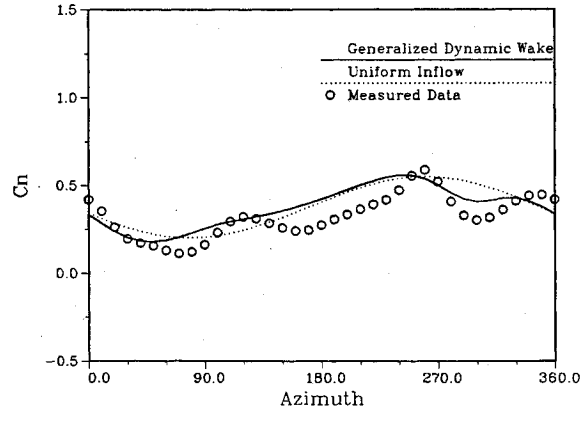

b) r = 0.88

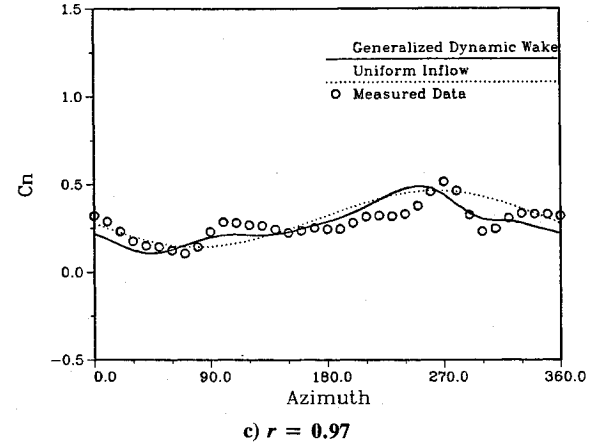

c) r = 0.97

Fig. 4 Normal force coefficient variation, C_T = 0.0042, μ = 0.140.

that of the test. For μ = 0.344, the correlation is not as good as that for the lower speed cases. Although both data and predictions show higher harmonic variations, they are underpredicted by the theory.

Lift Coefficient Prediction

Figure 4 shows the correlation of blade sectional normal force coefficient for μ = 0.14. Predictions based on uniform inflow model and dynamic wake are also compared. At r = 0.75, the predicted variation agrees with measured data very well. For the other two radial locations close to the tip, the theoretical predictions follow the data trend, but have smaller 2/rev and 4/rev variations than are seen in the measured data. Both calculated and measured results show a lift decrease on the advancing side and an increase on the retreating side. The figures also show the unsteady wake influence on blade air

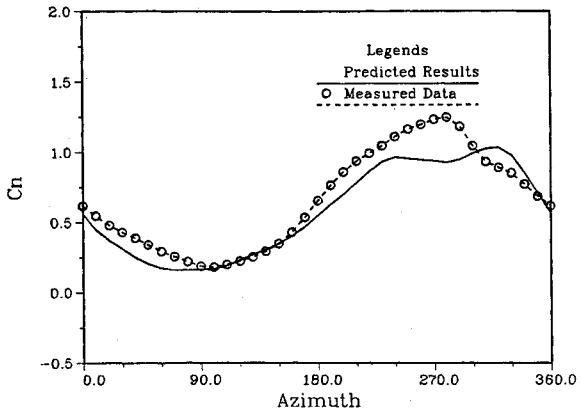

a) $r = 0.75$

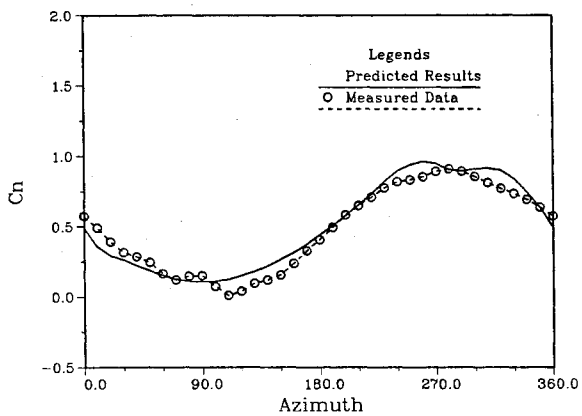

b) $r = 0.88$

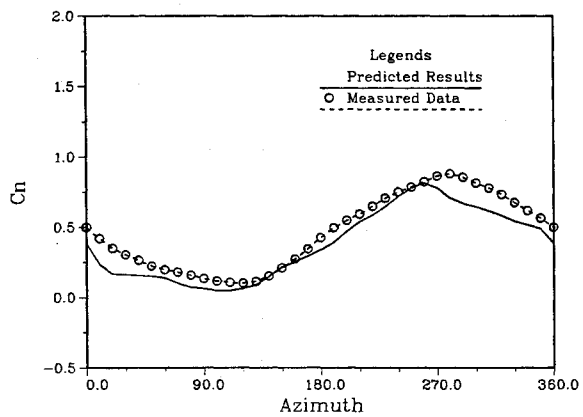

c) $r = 0.97$

Fig. 5 Normal force coefficient variation, $C_T = 0.0040$, $\mu = 0.344$.

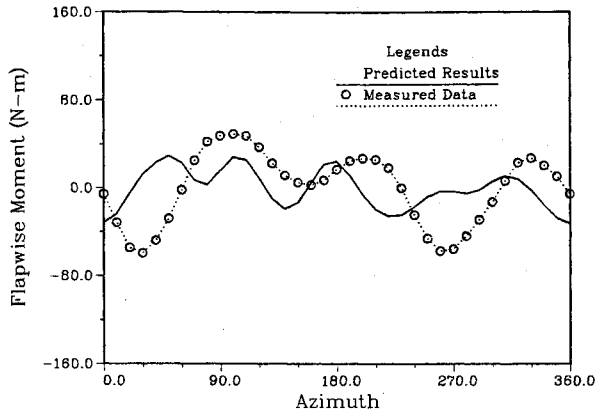

a) $r = 0.29$

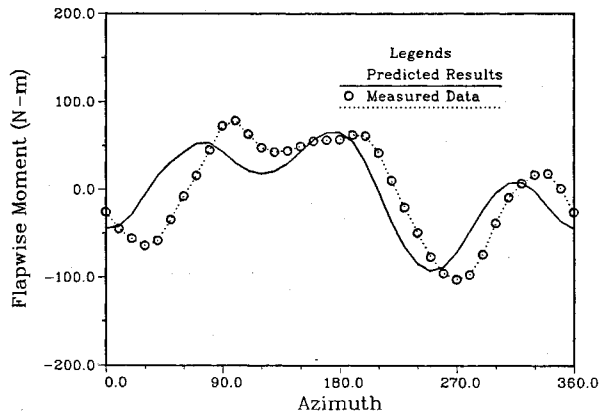

b) $r = 0.54$

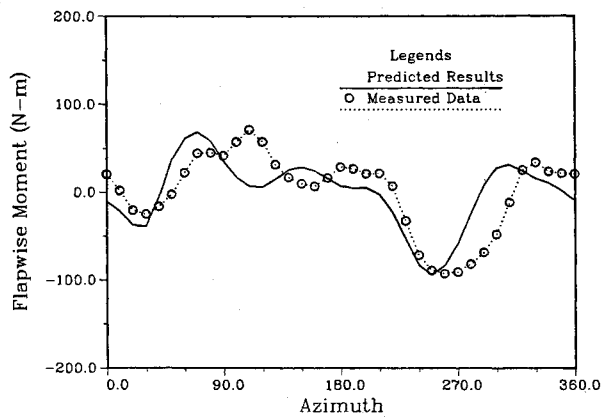

c) $r = 0.80$

Fig. 6 Vibratory flapwise moment variation, $C_T = 0.0040$, $\mu = 0.344$.

loadings. Inclusion of dynamic wake improves the correlation in several important regions, such as the 4/rev component and variation around $\psi = 90$ and 270 deg. This improvement is more obvious toward the blade tip region where the wake effect is believed to be greater.

Finally, Fig. 5 presents the correlation at a higher advance ratio, $\mu = 0.344$. Good agreement with measured data is obtained except in the region around $\psi = 270$ deg for $r = 0.75$.

Structural Bending Loads

Structural bending moments at different spanwise positions are calculated using the modal method where the product of curvature and bending stiffness gives the bending loads at a radial station. The flapwise bending moments are plotted in Fig. 6 at three different spanwise stations ($r = 0.29$, 0.54, and 0.80). The calculation has used nine blade modes and eight harmonics of induced flow.

A good agreement has been obtained outboard of $r = 0.30$. The edgewise bending moment for this case is shown in Fig. 7. The calculated results display a larger 5/rev (the natural frequency of the second lag mode) response than do the measured results. It is believed that a better lag damper model is needed for further improvement. However, a concern is the lack of 1/rev correlation in the edgewise moment. The source of this discrepancy is possibly due to the trim error. This requires further study, but should not affect the higher harmonic loads from the wake, which are the major concern of our new aerodynamic model.

To study the effect of induced flow modeling on the blade structural loadings, Fig. 8 compares results from two analytical models against the measured data. One set of results applies the generalized dynamic wake, and the other uses only

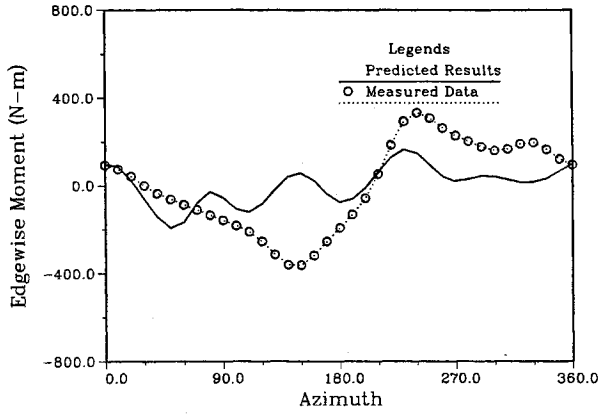

a) $r = 0.29$

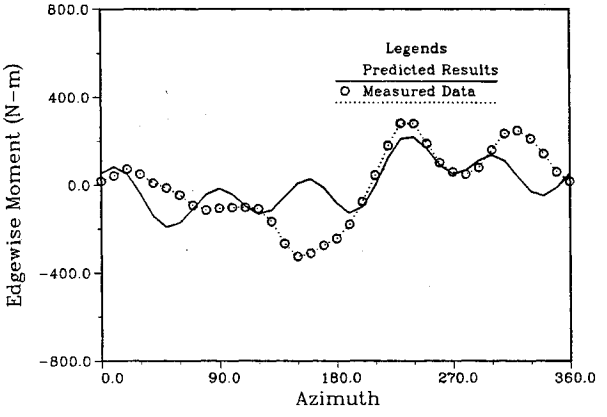

b) $r = 0.54$

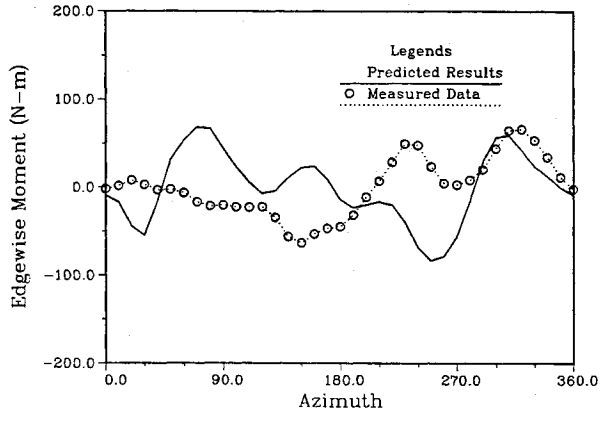

c) $r = 0.85$

Fig. 7 Vibratory edgewise moment variation, $C_T = 0.0040$, $\mu = 0.344$.

uniform-induced flow. An improvement from the inclusion of dynamic wake over the simple uniform induced flow is that a higher harmonic content is added to the response that is not present without the wake. Although the 1/rev force due to Glauert term can influence trim, it will not affect higher harmonic vibrations.[6] These higher harmonic contents come from higher harmonic inflow. However, the lack of phase correlation indicates that there are other higher harmonic contributions not modeled. These are probably due to the pitching moment anomaly between all present theories and flight test data as documented in Ref. 18. The generalized dynamic wake gives higher harmonic oscillations in both flapwise and edgewise bending moments as indicated in the measured data, while the uniform induced flow fails to show these.

Since the generalized dynamic wake approach involves truncation of induced flow expression in both harmonics and

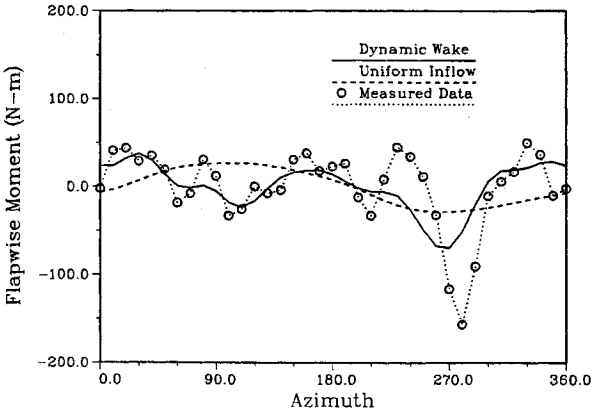

a) $C_T = 0.0042$, $\mu = 0.140$, $r = 0.85$

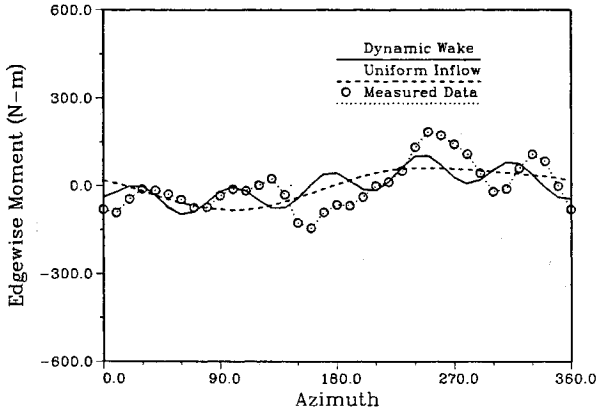

b) $C_T = 0.0042$, $\mu = 0.140$, $r = 0.54$

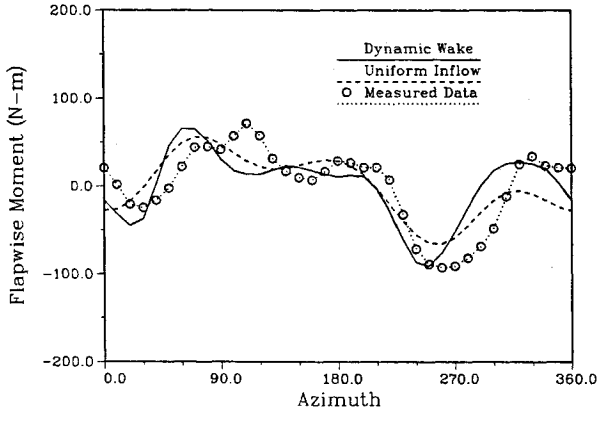

c) $C_T = 0.0040$, $\mu = 0.344$, $r = 0.80$

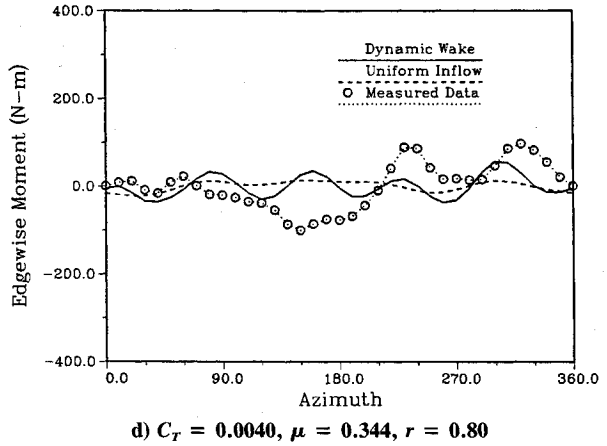

d) $C_T = 0.0040$, $\mu = 0.344$, $r = 0.80$

Fig. 8 Influence of induced flow modeling.

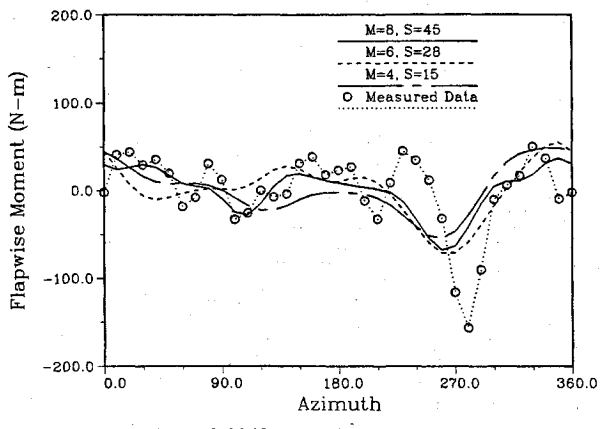

a) $C_T = 0.0042$, $\mu = 0.140$, $r = 0.85$

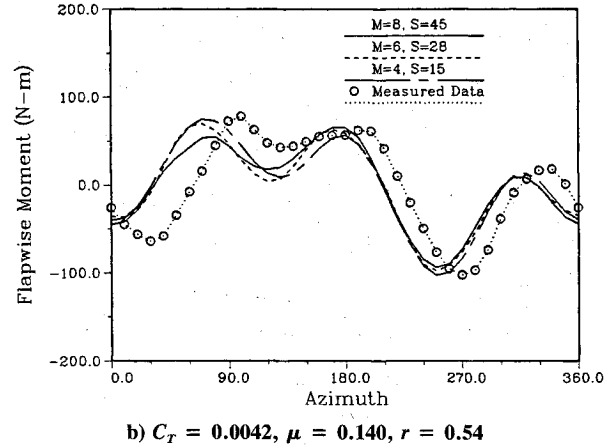

b) $C_T = 0.0042$, $\mu = 0.140$, $r = 0.54$

Fig. 9 Convergence of induced flow modeling.

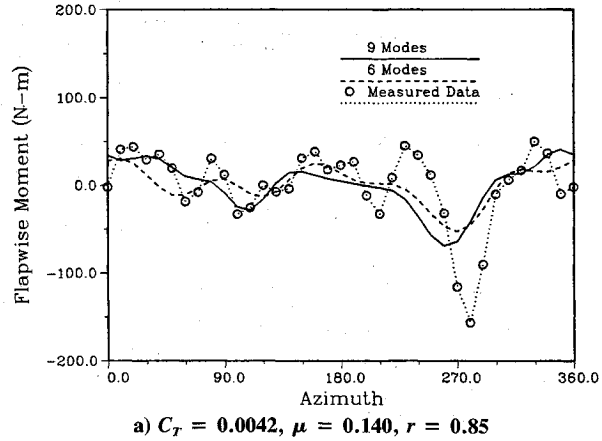

a) $C_T = 0.0042$, $\mu = 0.140$, $r = 0.85$

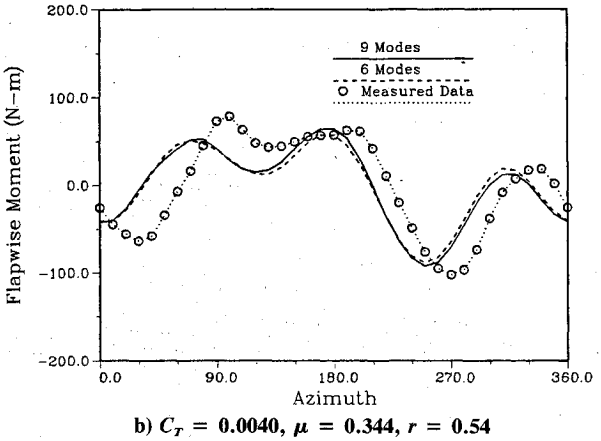

b) $C_T = 0.0040$, $\mu = 0.344$, $r = 0.54$

Fig. 10 Effect of number of blade modes.

radial shape functions, Fig. 9 investigates the convergence of the inflow modeling. Results are presented from three different truncations based on the optimum choice of the number of inflow radial shape functions.[12] The solid line is for 8 harmonics of induced flow with 45 inflow states; the dash line for 6 harmonics with 28 inflow states; and, finally, the chain dash line is for 4 harmonics with 15 inflow states. As seen, for the case of $\mu = 0.14$, Fig. 9a, four harmonics predicts the basic trend in the data, but more inflow harmonics help to improve the correlation. Although eight harmonics gives better predictions for the higher frequency variations, six harmonics gives reasonably converged results. Since the wake influence decreases with the forward flight speed, four harmonics of inflow dynamics seems to be sufficient for well-converged results at $\mu = 0.344$ in Fig. 9b.

Finally, Fig. 10 shows the results of using different numbers of structural modes. The case of nine blade modes (five flapping, two lag, and two torsion) gives only a slight improvement on higher harmonic variation. From the point of view of computational efficiency, the use of six blade modes is well-justified in this application.

Concluding Remarks

An aeroelastic model has been developed that couples a blade finite element analysis with finite state dynamic wake for rotorcraft multidisciplinary optimization design. The aeroelastic model can predict the blade airloads with an accuracy comparable to present state-of-the-art design tools. As a further improvement of the model in its aerodynamic aspects, a dynamic stall model needs to be added in order to be capable of modeling airfoil nonlinear aerodynamic properties. The model predicts the basic characteristics of the structural loads. For improvement, a better lag damper model is needed. In this application, a consistent aeroelastic modeling with six harmonics of inflow dynamics and six structural modes gives well-converged results. The unsteady rotor wake is one of the important sources of rotor vibratory loads, and thus it needs to be included in integrated optimization design.

Acknowledgment

This research work is supported by Interdisciplinary Research Division, NASA Langley Research Center under Grant NAG-1-710. Howard Adelman is the technical monitor.

References

[1]Johnson, W., "A Comprehensive Analytical Model of Rotorcraft Aerodynamics and Dynamics," NASA TM 811812, June 1980.

[2]Bir, G. S., Chopra, I., and Nguyen, K., "Development of UMARC (University of Maryland Advanced Rotorcraft Code)," *Proceedings of 46th Annual Forum of American Helicopter Society*, Vol. I, Washington, DC, May 1990, pp. 55–78.

[3]Hodges, D. H., and Dowell, E. H., "Nonlinear Equations of Motion for the Elastic Bending and Torsion of Twisted Nonuniform Rotor Blades," NASA TN D-7818, Dec. 1974.

[4]Friedman, P. P., "Formulation and Solution of Rotary-Wing Aeroelastic Stability and Response Problems," *Vertica*, Vol. 7, No. 2, 1983, pp. 101–104.

[5]Peters, D. A., Chouchane, M., and Fulton, M., "Use of an Optimized Controller and a Finite-State Stall Model to Find Trimmed Helicopter Controls," *Proceedings of 15th European Rotorcraft Forum*, International European Committee, Paper 44, Amsterdam, The Netherlands, Sept. 12–15, 1989.

[6]Yen, J. G., Yuce, M., Chao, C.-F., and Schillings, J., "Validation of Rotor Vibratory Airloads and Application to Helicopter Response," *Journal of the American Helicopter Society*, Vol. 35, No. 4, 1990, pp. 63–71.

[7]Friedman, P. P., "Application of Modern Structural Optimization Reduction in Rotorcraft," *Vertica*, Vol. 9, No. 4, 1985, pp. 363–373.

[8]Davis, M. W., and Weller, W. H., "Application of Design Optimization Techniques to Rotor Dynamics Problems," *Journal of the American Helicopter Society*, Vol. 33, No. 3, 1988, pp. 42–50.

[9]Lim, J. W., and Chopra, I., "Aeroelastic Optimization of a Helicopter Rotor," *Journal of the American Helicopter Society*, Vol. 34, No. 1, 1989, pp. 52–62.

[10]Chattopadhyay, A., Walsh, J. L., and Riley, M. F., "Integrated Aerodynamic/Dynamic Optimization of Helicopter Rotor Blades," NASA TM-101553, Feb. 1989.

[11]Peters, D. A., and He, C., "Correlation of Measured Induced Velocities with a Finite-State Wake Model," *Journal of the American Helicopter Society*, Vol. 37, No. 3, 1991, pp. 59–70.

[12]He, C., "Development and Application of a Generalized Dynamic Wake Theory for Lift Rotors," Ph.D. Dissertation, School of Aerospace Engineering, Georgia Inst. of Technology, Atlanta, GA, July 1989.

[13]Heffman, R., and Gaubert, M., "Structural and Aerodynamic Loads and Performance Measurements of a SA349/2 Helicopter with an Advanced Geometry Rotor," NASA TM88370, Nov. 1986.

[14]Ko, T., "Design of Helicopter Rotor Blades for Optimum Dynamic Characteristics," M.S. Thesis, Washington Univ., St. Louis, MO, Aug. 1984.

[15]He, C., and Peters, D. A., "An Aeroelastic Analysis with a Generalized Dynamic Wake," *Proceedings of the American Helicopter Society International Technical Specialists' Meeting on Rotorcraft Basic Research*, Paper 19, Atlanta, GA, March 1991, pp. 19-1–19-16.

[16]Johnson, W., *Helicopter Theory*, Princeton Univ. Press, Princeton, NJ, 1980, pp. 184–194.

[17]He, C., and Peters, D. A., "Analytical Formulation of Optimum Rotor Interdisciplinary Design with a Three Dimensional Wake," *Proceedings of 4th Air Force/AIAA/NASA Symposium on Multidisciplinary Analysis and Optimization*, Cleveland, OH, Sept. 1992, pp. 1164–1176.

[18]Bousman, W. G., Young, C., and Gilbert, N., "Correlation of Puma Airloads-Lifting Line and Wake Calculation," *Proceedings of 15th European Rotorcraft Forum*, International European Committee, Paper 21, Amsterdam, The Netherlands, Sept. 1989.